

1 **The relation among the ring current, subauroral polarization stream, and the**
2 **geospace plume: MAGE Simulation of the March 31 2001 Super Storm**

3
4 **Shanshan Bao¹, Wenbin Wang², Kareem Sorathia³, Viacheslav Merkin³, Frank Toffoletto¹,**
5 **Dong Lin², Kevin Pham², Jeffrey Garretson³, Michael Wiltberger², John Lyon⁴ and Adam**
6 **Michael³**

7 ¹Department of Physics and Astronomy, Rice University, Houston TX

8 ²High Altitude Observatory, National Center for Atmospheric Research, Boulder CO

9 ³Applied Physics Laboratory, Johns Hopkins University, Laurel MD

10 ⁴Department of Physics and Astronomy, Dartmouth College, Hanover NH

11 Corresponding author: Shanshan Bao (shanshan.bao@rice.edu)

12 **Key Points:**

- 13 • The first whole geospace simulation to demonstrate coherent storm-time evolution of
14 plasmaspheric and total electron content (TEC) plumes.
15 • The model demonstrates plasmasphere erosion and TEC depletion by the subauroral
16 polarization streams (SAPS).
17 • SAPS is sustained by magnetospheric ion and electron distributions formed by a delicate
18 balance of energy-dependent and $\mathbf{E} \times \mathbf{B}$ drifts.

19
20

21 Abstract

22 The geospace plume, referring to the combined processes of the plasmaspheric and the
23 ionospheric storm-enhanced density (SED)/total electron content (TEC) plumes, is one of the
24 unique features of geomagnetic storms. The apparent spatial overlap and joint temporal evolution
25 between the plasmaspheric plume and the equatorial mapping of the SED/TEC plume indicate
26 strong magnetospheric-ionospheric coupling. However, a systematic modeling study of the
27 factors contributing to geospace plume development has not yet been performed due to the lack
28 of a sufficiently comprehensive model including all the relevant physical processes. In this
29 paper, we present a numerical simulation of the geospace plume in the March 31, 2001 storm
30 using the Multiscale Atmosphere Geospace Environment model. The simulation reproduces the
31 observed linkage of the two plumes, which, we interpret as a result of both being driven by the
32 electric field that maps between the magnetosphere and the ionosphere. The model predicts two
33 velocity channels of sunward plasma drift at different latitudes in the dusk sector during the
34 storm main phase, which are identified as the sub-auroral polarization stream (SAPS) and the
35 convection return flow, respectively. The SAPS is responsible for the erosion of the
36 plasmasphere plume and contributes to the ionospheric TEC depletion in the midlatitude trough
37 region. We further find the spatial distributions of the magnetospheric ring current ions and
38 electrons, determined by a delicate balance of the energy-dependent gradient/curvature drifts and
39 the $E \times B$ drifts, are crucial to sustain the SAPS electric field that shapes the geospace plume
40 throughout the storm main phase.

41 1 Introduction

42 During geomagnetically active times, multiscale dynamic processes are triggered
43 throughout the magnetosphere, the ionosphere and the thermosphere in response to the solar
44 wind driving. Once the global magnetospheric convection initiates, the ring current starts to
45 accumulate, reshaping the global structure of the magnetosphere and establishing a distinctive
46 dynamic storm-time pattern of the electromagnetic field and plasmas. The Imager for
47 Magnetopause-to Aurora Global Exploration (IMAGE) satellite observed the dynamic evolution
48 of the cold ($\sim 1\text{eV}$) and dense ($\sim 10^4/\text{cc}$) plasmasphere (Lemaire et al., 1998) and the sunward
49 extension of a plume-like high density structure from the dusk edge of the plasmasphere (the
50 “drainage plume”) through the EUV images (Burch et al., 2001; Sandel et al., 2001; Goldstein,
51 2004; Goldstein & Sandel, 2005). The IMAGE satellite also detected, through the high-energy
52 neutral atom (HENA) images, that the spatial distribution of the partial ring current roughly
53 complements the shape of the plasmapause (Pulkkinen et al., 2005; Goldstein, 2007). In the
54 ionosphere, the storm-time electron density enhancement at low to midlatitudes in the day and
55 dusk sectors is a prominent feature known as a “positive storm effect” (Liu et al., 2016;
56 Fagundes et al., 2016). Furthermore, a plume-like high total electron content (TEC) structure
57 extends from the positive storm effect region in the noon-to-dusk sector toward higher latitudes
58 and into the polar cap, which is commonly observed by incoherent scatter radars, ground-based
59 Global Positioning System (GPS) measurements and near-Earth satellites (e.g., Foster, 1993;
60 Zou et al., 2013, 2014; Foster et al., 2020). The term “geospace plume” has been used to refer to
61 the coupled, jointly evolving high plasma density structures including the plasmaspheric
62 drainage plume and the storm-enhanced density (SED)/TEC plume in the ionosphere (Foster et
63 al., 2020). Foster et al. (2002) first pointed out the “linkage” between the plasmaspheric plume
64 and the ionospheric SED/TEC plume by comparing the IMAGE EUV plasmasphere image and
65 the equatorial mapping of the GPS TEC map. They noted that the co-location of the plumes

66 indicates strong magnetosphere-ionosphere (MI) coupling. Further observations show that the
67 sub-auroral polarization stream (SAPS), a latitudinally narrow large plasma drift channel in the
68 sub-auroral ionosphere in the dusk-to-midnight sector (Foster & Burke, 2002), may play an
69 important role in shaping the dusk edge of the plasmasphere and further depleting the middle
70 latitude electron density trough in the ionosphere. In other words, the SAPS electric field maps
71 across the plasmopause on the dusk side causing strong westward ion transport and contributes to
72 the formation of the ionospheric electron density trough which is co-located with the SAPS
73 channel (Foster & Burke, 2002; Foster, 2002; Foster et al., 2007, 2014; Zou et al., 2021).

74
75 Numerical simulations of the geospace plume system have been conducted along with the
76 observational studies. Goldstein et al. (2003, 2005, 2014) used cold test particles at the
77 plasmopause that were driven by empirical convection and an ad-hoc SAPS electric potential to
78 track the plasmasphere evolution. They found that the SAPS electric field is crucial in order to
79 reproduce the storm-time, dusk-side structures of the plasmasphere, such as the plasmopause
80 radius and the plasmaspheric plume. The first 3D simulation of the plasmasphere was conducted
81 using the SAMI3 model that was driven by an empirical electrostatic potential (Huba & Krall,
82 2013). The study found that the simulated plasmasphere evolves from a toroidal symmetric shape
83 into a contracted size with a development of a plume-like structure after the storm. The
84 Thermosphere Ionosphere Electrodynamics General Circulation Model (TIEGCM) (Richmond et
85 al., 1992; Qian et al., 2014) has been extensively used to investigate thermosphere-ionospheric
86 response to geospace disturbances and SAPS. For example, C. H. Lin et al. (2005) used the
87 TIEGCM with the $\mathbf{E} \times \mathbf{B}$ drift derived from satellite measurements of the ion velocity to study the
88 relative importance of winds and electric field for low and midlatitude electron density
89 enhancements. Wang et al. (2012) and Lu et al. (2020) used a synthetic SAPS electric field
90 model to investigate the response of neutral winds, SED plume and traveling ionospheric
91 disturbances to SAPS. SAMI3 coupled with the Rice Convection Model (RCM) of the inner
92 magnetosphere was used to simulate the evolution of the ionosphere-plasmasphere system and
93 demonstrated the linkage between the plasmaspheric plume and the mapped SED/TEC plume
94 during a geomagnetic storm (Huba & Sazykin, 2014, 2017).

95
96 In recent years, magnetosphere-ionosphere-thermosphere (M-I-T) coupled models have
97 been developed and used to simulate SAPS (Raeder et al., 2016; Lin et al., 2019, 2021, 2022).
98 These studies showed that the coupled geospace models can capture the complex interactions
99 and feedback loops in the M-I-T system and reproduce the distinctive features of SAPS in
100 observations. Yet, such coupled models have not yet been used to study the geospace plume.
101 Most of the previous modeling studies simulated the plasmaspheric plume and the ionospheric
102 SED/TEC plume separately, precluding studies that would elucidate the physics underlining the
103 linkage between the two plumes. The use of ad-hoc or empirical SAPS electric field instead of
104 self-consistent, physics-based SAPS modeling prevents an investigation of the magnetosphere-
105 ionospheric coupling processes involved, where the coupled processes of the ring current
106 buildup, the Region-2 current generation and the electron precipitation could play important
107 roles in the generation of SAPS (Lin et al., 2021, 2022) and the plume dynamics. SAMI3-RCM
108 simulation (Huba & Sazykin, 2014, 2017) had the advantage of a common electromagnetic field
109 driving both ionospheric and magnetospheric plumes in the closed-field-line region, but it lacked
110 a physics-based representation of high-latitude dynamics coupled to the rest of the simulation
111 domain and an outer-magnetosphere model that can provide the ring current model with storm-

112 time plasma injections at its boundary (Bao et al., 2021; Cramer et al., 2017; De Zeeuw et al.,
113 2004; Lin et al., 2021; Pembroke et al., 2012).

114

115 In this study, we use such a coupled M-I-T model to gain a comprehensive understanding
116 of the geospace plume evolution during storm-times. We address three science questions: (1)
117 What is the cause of the linkage between the plasmaspheric plume and the ionospheric SED/TEC
118 plume? (2) What specific processes are important for shaping the geospace plume? (3) What is
119 the relation between the ring current build-up and the geospace plume development? For this
120 purpose, we employ the Multiscale Atmosphere-Geospace Environment (MAGE) model (Lin et
121 al., 2021, 2022; Pham et al., 2022) to simulate the multiscale dynamics throughout the outer and
122 inner magnetosphere, the ionosphere and the thermosphere to determine the relevant correlations
123 and potential causal relationships. The coupled whole geospace model requires a number of key
124 components. First is the global magnetospheric MHD model that can capture both global and
125 inner magnetospheric dynamics such as large-scale storm-time magnetospheric convection and
126 particle gradient/curvature drifts and provide self-consistent dynamic magnetic field
127 configuration along with the associated current system. A coupled thermosphere-ionospheric
128 model is also needed to not only self-consistently evolve the upper atmospheric neutral species
129 but also simulate ionospheric electron densities, and provide ionospheric conductance to solve
130 the current continuity equation for the global ionospheric electrostatic potential. Finally, the
131 model must include the coupling of FACs, particle precipitation, ionospheric conductance, and
132 ionospheric electric field to ensure feedback and self-consistency within the entire geospace
133 system.

134 **2 The MAGE model**

135 The MAGE model used in this study provides a comprehensive and self-consistent
136 description of multiscale physical processes in the different domains of geospace. The current
137 version of MAGE (1.0) couples the global magnetosphere, the inner magnetosphere, the
138 ionosphere and the thermosphere (Lin et al., 2021, 2022; Pham et al., 2022). As shown in Figure
139 1, the global magnetospheric MHD model, Grid Agnostic MHD with Extended Research
140 Applications (GAMERA) model (Zhang et al., 2019; Sorathia et al., 2020) solves the single-fluid
141 MHD equations and passes FACs to the ionosphere potential solver, and the RE-developed
142 Magnetosphere-Ionosphere Coupler/Solver (REMIX) which is a rewrite of the Magnetosphere-
143 Ionosphere Coupler/Solver (MIX) code (Merkin & Lyon, 2010). REMIX solves the electric
144 potential for both hemispheres. The GAMERA plasma moments and electromagnetic field are
145 passed to the Rice Convection Model (RCM), the inner magnetosphere ring current model
146 (Toffoletto et al., 2003), to evolve the drifting plasma distribution in the form of multiple-fluids
147 with different energy invariants. The plasmasphere is modeled as a zero-energy proton channel
148 in RCM and follows the $\mathbf{E} \times \mathbf{B}$ drift including corotation. The plasmasphere is initialized with a
149 2D density profile as a function of the Kp index modified from the 1D Gallagher model
150 (Gallagher et al., 2000). The total plasma density and pressure are fed back to the GAMERA
151 model. There are also two kinds of electron precipitation simulated by the current MAGE model:
152 the RCM-computed diffuse electron precipitation, i.e., pitch-angle scattered electrons falling into
153 the loss cone (Wolf, 1983; Bao, 2019), and the GAMERA-computed mono-energetic electron
154 precipitation accelerated by field-aligned potential drops (Zhang et al., 2015). The electron
155 precipitation and the electric potential are used as input to the TIEGCM that calculates the
156 density, temperature and transport of electrons, ions, and neutrals. The electron precipitation,

157 along with the solar EUV radiation, produces ionization in the ionosphere and the ionospheric
 158 conductivity.

159
 160 Two important physical processes are not yet included in MAGE and therefore are not
 161 addressed in this study. The first is a physics-based representation of the plasmaspheric refilling
 162 process. In the current version of MAGE, we model the plasmasphere inside the inner-
 163 magnetosphere model, RCM, with a simple empirical refilling model being used, whereas the
 164 ionospheric electron density is solved separately in a coupled thermosphere-ionospheric model,
 165 TIEGCM. Specifically, in this study, the refilling model is in fact turned off to isolate the effects
 166 of electrodynamic coupling and investigate whether the linkage of the two plumes still exists
 167 without mass exchange. Plasmasphere refilling is a slow process (\sim days) compared with the
 168 storm-time plasmaspheric density changes (\sim hours) (Lawrence et al., 1999; Denton et al., 2012;
 169 Krall et al., 2014) and the exclusion of the refilling should not fundamentally change the storm-
 170 time plasmaspheric dynamics.

171

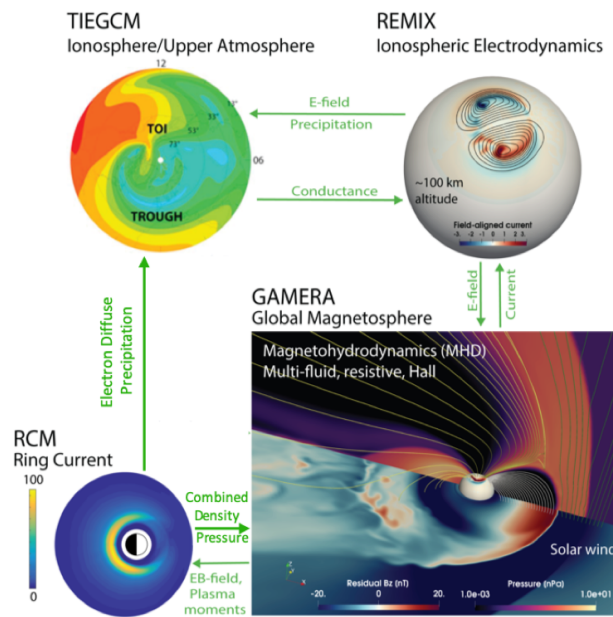


Figure 1. Diagram of the MAGE components and their coupling in this study.

172

173 2.1 Simulation Setup

174 The event studied in the paper is the super storm that occurred on March 31, 2001. The
 175 super storm was a result of a coronal mass ejection event that caused the SYM/H index to reach -
 176 400 nT. Figure 2 shows the solar wind profile, including, from top to bottom, the dynamic ram
 177 pressure, the solar wind velocity components, the interplanetary magnetic field (IMF)
 178 components, and the SYM/H index, extracted from the NASA/GSFC's OMNI dataset through
 179 CDAWeb. There are two periods of southward (SW) IMF, the first, 03:00~08:00UT 03-31-2001,
 180 which was followed by a period of northward IMF, and the second, 15:00~22:00UT. The
 181 simulation covered the entire storm, but our analysis focuses mostly on the geospace plume
 182 development in the first period of the southward IMF (highlighted in Figure 2 in blue shade).

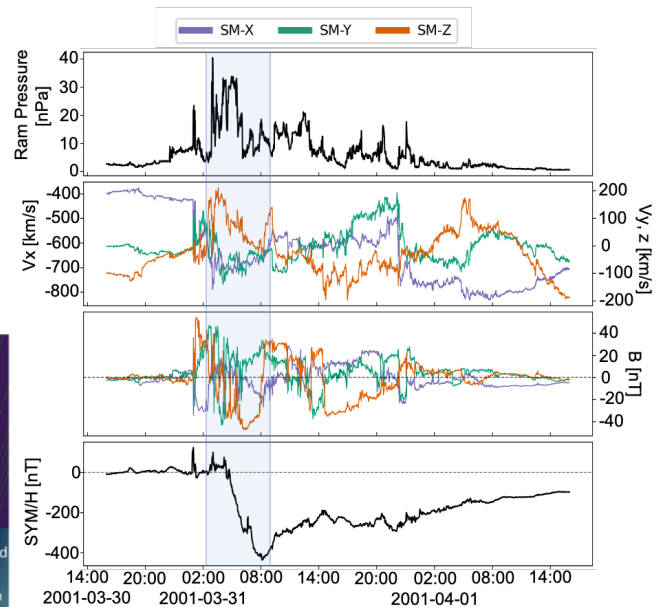


Figure 2. Solar wind dynamic pressure and velocity (top two panels), IMF components (third panel), and the SYM-H index (bottom panel) during the March 31, 2001, super storm. Data source: CDAWeb/NASA

183
 184 In this work, we use the so called ‘Quad’ resolution for GAMERA, which corresponds to
 185 96, 96, and 128 grid cells in radial, meridional and azimuthal directions (the spherical axis of the
 186 grid is aligned with the Solar Magnetic (SM) x-axis). The non-uniform 3D grid is much denser in
 187 the inner magnetosphere region with its inner boundary set at $1.5R_E$. The REMIX 2D grid is
 188 $1^\circ \times 1^\circ$ in longitude and latitude with a low latitude boundary at 35° magnetic latitude (MLAT).
 189 The RCM 2D physical grid is $1^\circ \times 1/3^\circ$ in longitude and latitude and for the energy grid, it uses 1
 190 energy channel for the plasmasphere, 29 energy channels for the electrons and 84 energy
 191 channels for the protons. Oxygen channels are not used in this study. GAMERA, REMIX and
 192 RCM grids are defined in the SM coordinates. The TIEGCM 3D grid covers the entire globe and
 193 is defined in the geographic coordinates. Its resolution is $1.25^\circ \times 1.25^\circ$ in longitude and latitude
 194 and it has 57 levels of vertical pressure grid (1/4 scale height resolution), ranging from ~ 97 km to
 195 approximately 900 km. The coupling exchange interval between GAMERA and REMIX is 5 s,
 196 while for GAMERA and RCM, the exchange interval is 15 s and for REMIX and TIEGCM, it is
 197 5 s. The MAGE simulation starts at 16:00 UT, March 30, 2001 and lasts for 48 hours.

198 3. Overview of the simulation results

199 The evolution of the geospace plume is shown in Figure 3 through different stages of the
 200 storm (specifically for the 1st period of the southward IMF in Figure 2). The entire process of
 201 geospace plume development is demonstrated in Movies S1 and S2. In Figure 3(a1)-(a5) (the
 202 first row) and (d1)-(d5) (the fourth row), we map the relevant processes onto the magnetic
 203 equatorial plane defined as the surface of minimum magnetic field. The plasmapause as the
 204 100/cc iso-surface of the cold proton density. The colored areas are within the closed-field-line
 205 region and the blanked areas are for the open-field-line region. The electric potential ϕ plotted in
 206 the equatorial plane is a combination of the ionospheric electrostatic potential ϕ_I and the
 207 corotation potential ϕ_c , defined as

$$208 \quad \phi = \phi_I + \phi_c \quad (1)$$

$$209 \quad \phi_c = -\frac{\omega_E B_0 R_E^3}{r} \quad (2)$$

210 where r is the radial distance; ω_E is the angular speed of the Earth’s rotation; B_0 is the strength of
 211 the Earth’s dipole moment; R_E is the radius of the Earth (Toffoletto et al., 2003). The contours of
 212 the electric potential represent the streamlines of the plasma $\mathbf{E} \times \mathbf{B}$ drift flow. Here, the
 213 ionospheric electrostatic potential ϕ_I is calculated by REMIX and shown in Figure 3(b1)-(b5)
 214 (the second row). The ionospheric potential calculated by TIEGCM is shown in Figure(c1)-(c5)
 215 (the third row), where it uses the electric potential from REMIX in the high latitude region
 216 (MLAT > 60) and solves for global ionospheric potential including the neutral wind dynamo. All
 217 the ionospheric plots in this paper are for the northern hemisphere.
 218
 219

220 At the pre-storm stage (Figures 3(a1)-(d1), the first column), both the FACs and the
 221 ionospheric electric potential are weak. The co-rotation electric field dominates and drives the
 222 plasmasphere co-rotate with the Earth, with the plasmapause around $3.5 \sim 4R_E$ (bottom row,
 223 Figure 3(d1) The ionospheric TEC peaks near 20 MLAT with a value of ~ 140 TECu and has a
 224 higher value (> 50 TECu) in the noon-to-dusk sector from low- to midlatitude than in the
 225 midnight-to-dawn sector.
 226

227 Around 02:30~04:30UT, 03-31-2001, the impact of the CME event arrives at Earth, with an
228 evident increase in the ram pressure and fluctuations in the IMF (Figure 2) causing the storm
229 initial phase. By the end of the initial phase (Figure 3(a2)-(d2), the second column) the solar
230 wind driving has caused the formation of the Region-1 current, while the Region-2 current is still
231 relatively weak. The two-cell convection pattern in the electric potential starts to establish and
232 this initiates global-scale sunward convection on the nights side (Figure 3(b2)), although the ring
233 current has not yet developed (Figure 3(a2)). From the extent of the dashed contour lines of the
234 potential in Figure 3(d2), we can see that a plume-like structure began to emerge in the
235 plasmasphere as well as in the middle-high latitude ionosphere. Specifically, the plasmasphere
236 starts to expand sunward and a finger-like structure (a plasmaspheric “finger”) starts to develop
237 at the dusk edge of the plasmopause (heavy line in Figure 3(d2)). We will briefly discuss its
238 cause in Section 4.2.1.

239
240 During the early main phase (Figure 3(a3)-(d3), the third column), the FACs and the
241 ionospheric convection electric fields become stronger (Figure 3(b3)). The Region-2 current is
242 enhanced due to a substantial ring current pressure accumulation (Figure 3(a3)). The peak of the
243 TEC has moved to 30 MLAT and a TEC plume occurs with ~ 70 TECu and expands toward the
244 polar cap from 45 MLAT to 75 MLAT near 14 MLT driven by the dusk-cell of the convection
245 (Figure 3(c3)). The plasmaspheric plume has formed, with the plasmasphere finger merged into
246 its main body (Figure 3(d3)). The shape of the plasmaspheric plume maintains approximate
247 dawn-dusk symmetry about the noon-midnight line in the equatorial plane.

248
249 In the late main phase (Figure 3(a4)-(d4), the fourth column), the strength of the ring
250 current reaches its maximum. Due to the westward drifting of the ion population, the ring current
251 pressure distribution is skewed toward pre-midnight (Figure 3(a4)). The FACs become much
252 more intense (Figure 3(b4)) causing stronger central convection electric field that enhances the
253 ionospheric-poleward/equatorial-sunward expansion of the geospace plume (Figure 3(b4), (c4)
254 and (d4)). The high TEC region due to the positive storm effect extends from 30 MLAT to 45
255 MLAT and 60 MLAT in the ionosphere (Figure 3(c4)) and it becomes the center of the TEC
256 plume on the equatorial plane (Figure 3(d4)). Meanwhile, the two-cell convection pattern is
257 skewed clockwise, where the dusk-side pair of the Region-1 and the Region-2 current is located
258 mostly in the afternoon sector and the dawn-side pair of the Region-1 and Region-2 current is
259 skewed to the pre-dawn sector (Figure 3(b4)). The clockwise twist of the convection pattern
260 reshapes the geospace plume. As shown in Figure 3(d4), the shape of the plasmasphere and the
261 TEC contour follows the shape of the potential contour lines. The potential contours show a
262 prominent dawn-dusk asymmetry. As positive storm effects occur primarily in the late afternoon
263 to dusk (~ 14 -19 MLT in Figure 3(c4)) at low and middle latitudes, the strong convection in the
264 dusk sector transport plasma toward high latitudes. The plume structure follows the potential
265 contours and the plume is biased to the dusk side. Another prominent feature during the main
266 phase is the presence of TEC depletion channels. In the dusk sector, a low TEC channel expands
267 from the equator and merges into the midlatitude (~ 45 MLAT) electron density/TEC trough
268 region. There is another low-TEC channel located around 60 MLAT inside the auroral oval. Both
269 TEC depletion channels (marked by red arrows in Figure 3(c4)) extend sunward. In the
270 equatorial plane, the midlatitude depletion channel is located at the dusk edge of the
271 plasmaspheric plume and we can see the plasmaspheric plume has become much narrower
272 compared with its shape in the early main phase. We refer to this depletion of the TEC and the

273 narrowing of the plasmaspheric plume as geospace plume “erosion”. We will discuss these two
274 features in Sections 4.2.2.

275
276 In the last stage, 08:00~12:00UT, 03-31-2001, which is the storm recovery phase (Figure
277 3(a5)-(d5), the fifth column), the IMF turns northward and the ram pressure decreases. The
278 ionospheric convection becomes much weaker (Figure 3(b5)). The two TEC depletion channels
279 merge into one and cut across the tongue of ionization and leaves some polar cap patches (Figure
280 3(c5)). In the equatorial plane (Figure 3(d5)), the sunward driving of the plasmaspheric plume
281 diminishes and the co-rotation takes over again. Due to the loss of the particles through the
282 dayside to the open-field-line region, the size of the plasmasphere shrinks significantly with a
283 plasmopause radius of $2 \sim 2.5R_E$.

284
285 There are three prominent features from the simulation results. The first is that the
286 equatorial plane mapping of the TEC colored contour resemble the shape of the plasmopause.
287 Especially during the storm's main phase, their synchronized sunward expansion and the overlap
288 of the two plumes is quite apparent. We will discuss the major cause of their linkage in Section
289 4.1. The second feature, as mentioned above, is the density depletion channels in the dusk sector
290 at midlatitude. We investigate their role in eroding the dusk edge of the plasmasphere plume in
291 Section 4.2. Thirdly, the ring current development with its dusk-preferred accumulation
292 significantly impacts the distribution of the FACs and thus the electric fields, which eventually
293 control to the geospace plume development. We investigate the relation between the ring current
294 build-up and the geospace plume evolution in detail in Section 4.3.

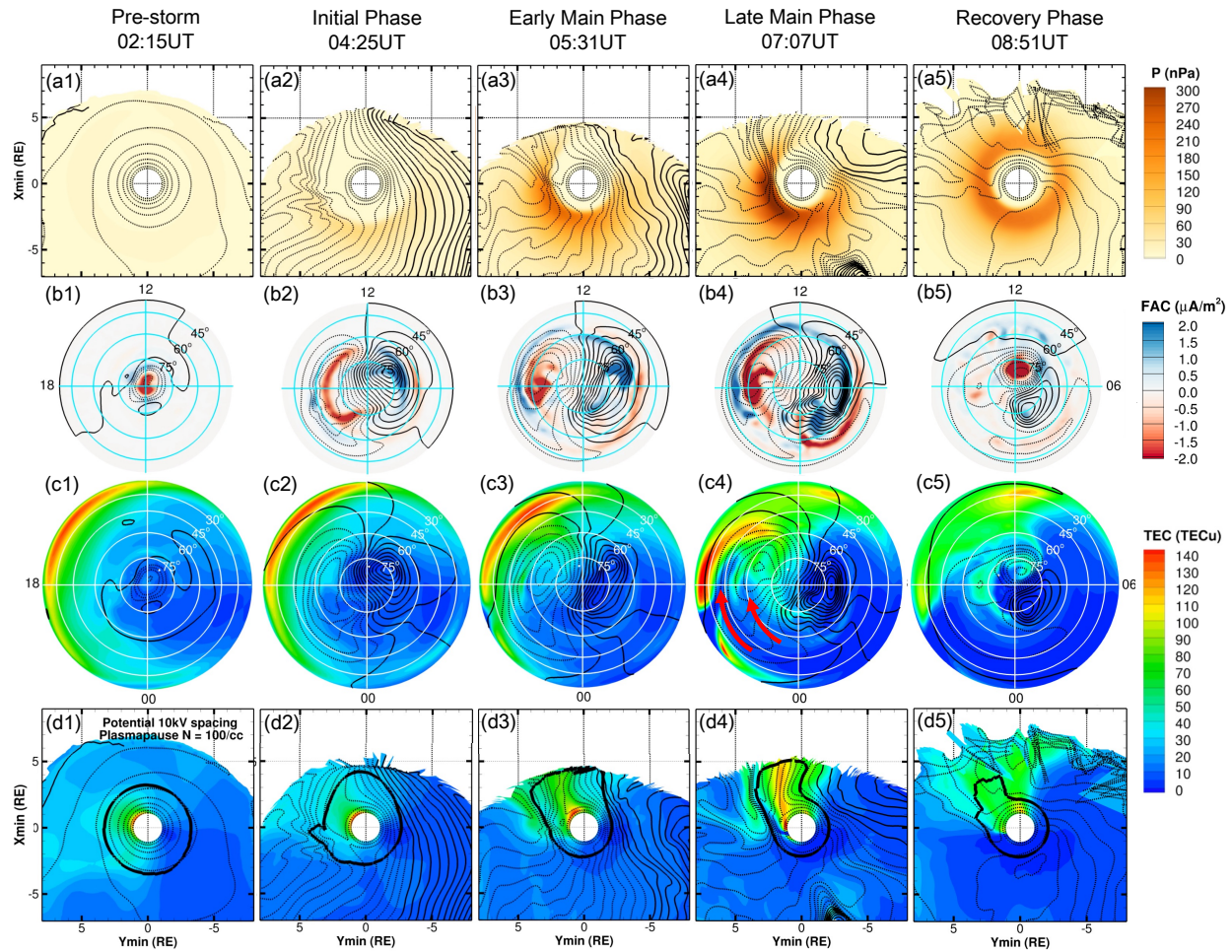


Figure 3. (a1)-(e1) to (a5)-(e5) show five stages of the storm (the 1st period of southward IMF shaded in Figure 2) with each column, top to bottom, depicting the equatorial plane view of the ring current pressure, the ionospheric FAC, the ionospheric TEC and the equatorial plane mapping of the TEC and the plasmopause (heavy black contour). The thin black lines (dashed for negative values) are contours of the electric potential, with 10keV interval on equatorial plane (bottom row) and 20keV in the ionosphere (third row from top).

295 **4. Discussion**

296 **4.1 Linkage between the plasmaspheric and the ionospheric plumes**

297 Foster et al. (2002) first reported the overlap of the plasmaspheric plume with the
 298 magnetospheric mapping of the ionospheric plume during the March 31, 2001 storm. The
 299 IMAGE satellite and the World-wide TEC measurement jointly observed the resemblance of the
 300 two plumes for the second period of the southward IMF. Figure 4(a) shows the IMAGE EUV
 301 image of the plasmasphere at 21:23UT, March 31, 2001 (Source: <http://euv.lpl.arizona.edu/euv/>).
 302 Figure 4(b) is the World-wide TEC data (Source: Madrigal database) mapped to the equatorial
 303 plane using the magnetic field-line traced in the MAGE model. Figures 4(a) and (b) are adjusted
 304 to a similar length scale as Figure 4 of Moldwin et al., 2016. The plasmopause is located at

305 approximately $2R_E$ on the nightside and the plasmaspheric drainage plume expands from the
 306 dusk edge of the plasmasphere toward the subsolar magnetopause (Figure 4(a)). The projection
 307 of the observed global TEC on the equatorial plane at 21:22UT (Figure 4(b)) shows similar
 308 shape and orientation with the plasmaspheric plume. Figure 4(c) gives the MAGE simulated
 309 plasmapause and TEC projected to the equatorial plane on the same color scale. The simulated
 310 plasmaspheric plume is co-located with the TEC plume which is consistent with the
 311 observations.
 312

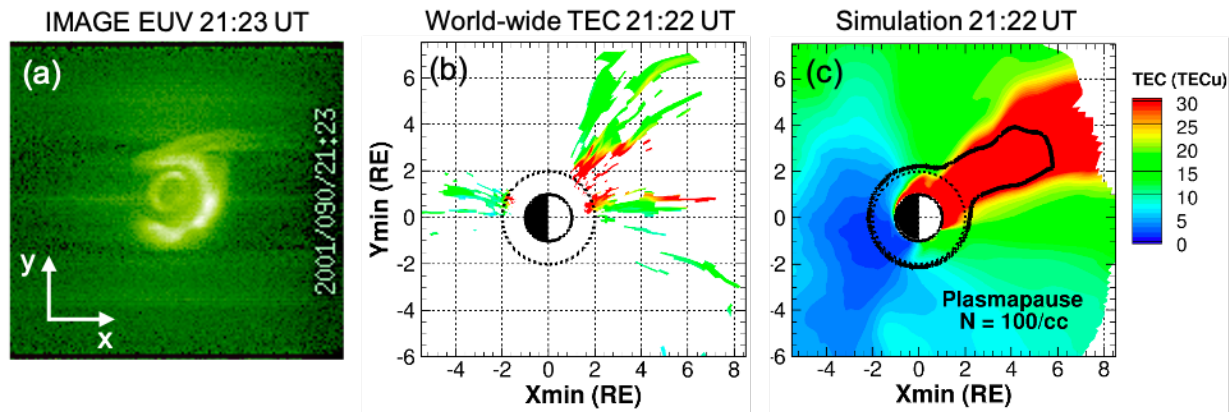


Figure 4. (a) IMAGE EUV image of the plasmasphere taken at 21:23UT, 03-31-2001. (b) The equatorial-plane projection of the global TEC measurement at 21:22UT, 03-31-2001, mapped by the MAGE magnetic field line. (c) The contour plot of the MAGE simulated plasmapause and TEC projection on the equatorial plane. The plasmasphere and the TEC are presented in SM coordinates. The sun is to the right. Black solid circle represents the Earth and the dashed black circle has a radius of $2R_E$.

313 This overlap in the equatorial mapping of the two plumes can be seen throughout the
 314 storm. As described in Section 3 and shown in Figure 4, both the plasmasphere and the electron
 315 content co-rotate eastward when the two-cell potential pattern has not yet been established.
 316 During the strong southward IMF driving, e.g., at $T = 650 \sim 950$ min in Movie S1, the
 317 ionospheric two-cell convection dominates over the co-rotation. The evolution of the plumes is
 318 controlled by the dusk cell and follows the geometry of local electric potential contours. In the
 319 noon-to-dusk sector, the plumes extend from the low middle latitudes to the pole, which
 320 corresponds to the sunward expansion in the equatorial plane.
 321

322 Compared to the SAMI3-RCM simulation of the same event (Huba & Sazykin, 2014), in
 323 our MAGE simulation, the plasmaspheric plume (from RCM) and the TEC (from TIEGCM)
 324 plume are driven by the midlatitude electric fields that are controlled by the same high-latitude
 325 electric field, but the mass exchange between the ionosphere and the plasmasphere is not
 326 included. However, the overlap and joint evolution of the two plumes are still successfully
 327 reproduced. This indicates that the electrodynamic coupling in the M-I-T system, rather than the
 328 mass connection, plays a dominant role in the formation and evolution of the geospace plume in
 329 both the plasmasphere and the ionosphere.
 330

331

4.2 Westward ion drifts (WIDs) and their effect on the geospace plume

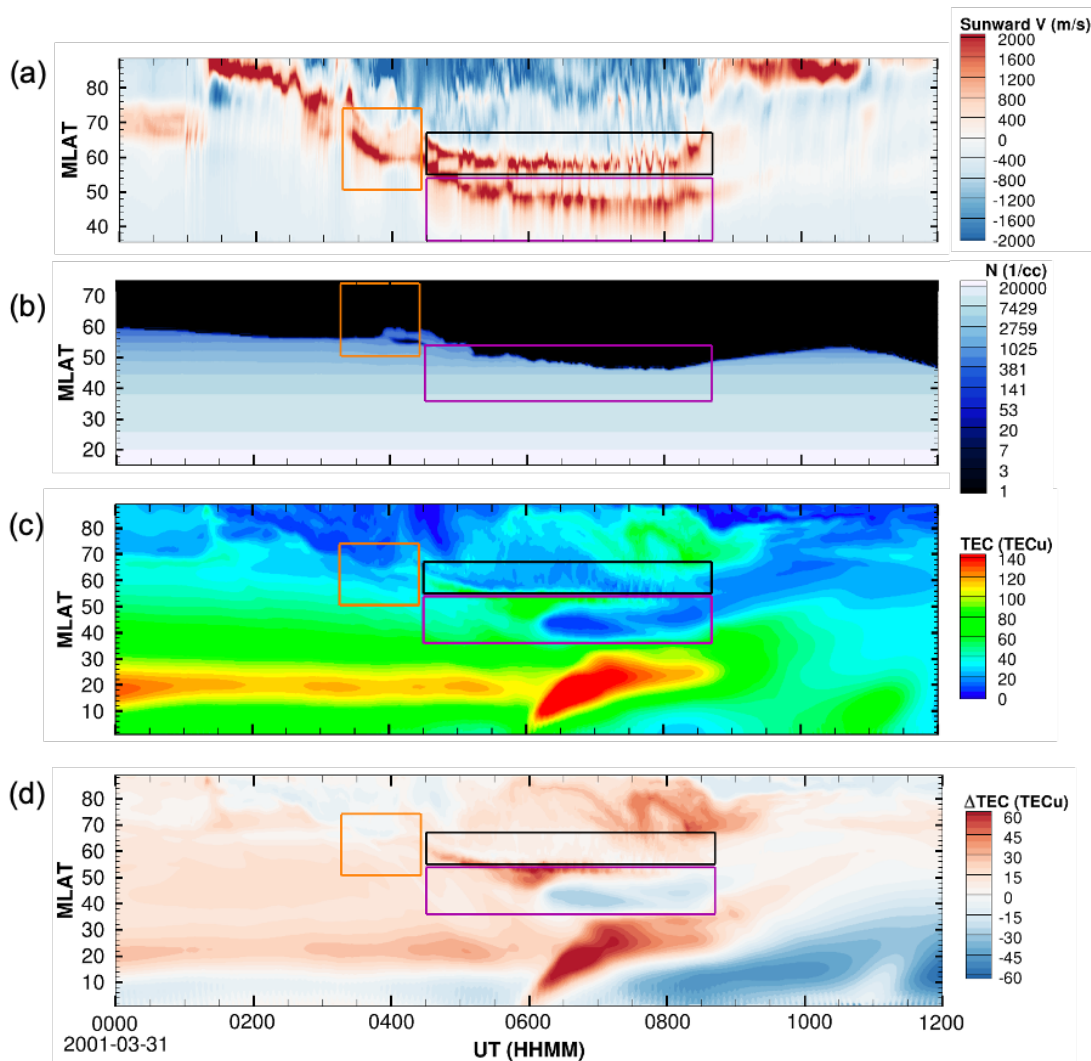


Figure 5. (a)-(d) Keograms of the simulated westward (sunward) ion drift velocity, plasmaspheric density, TEC and Δ TEC at 18 MLT. Δ TEC is calculated by subtracting the quiet-time (March 29, 2001) TEC from the storm-time TEC at the same UT. The colored boxes mark the sunward velocity peaks and the corresponding erosion region in the plasmaspheric density, TEC and Δ TEC. The boxes of the same color cover the same range of latitude in different panels. The orange box marks the WID in the initial phase; the purple box marks the WID velocity peak in the midlatitude; the black box marks the?????

332
333
334
335
336
337

To further investigate the geospace plume erosion on the dusk side, we sample the MAGE simulated ion drift velocity (from REMIX), ionospheric mapping of the plasmaspheric density (from RCM), TEC and Δ TEC (from TIEGCM) along 18 MLT for the first period of southward IMF (Figures 5(a) - (d)). The Y-axes of different panels cover different ranges of magnetic latitude since the variables are calculated in different MAGE component models. In Figure 5(a), the ion drift velocity is a combination of the corotation velocity and the $\mathbf{E} \times \mathbf{B}$ ion

338 drift velocity in the SM coordinates. The red color signifies a westward (i.e., sunward at 18
339 MLT) direction, while the blue color signifies an eastward/tailward direction.

340

341 4.2.1 The plasmasphere finger

342

343 During the initial phase (around 01:30~04:30UT), when the two-cell convection pattern
344 starts to establish, a single band of WID velocity peak moves from high latitude toward
345 midlatitude (Figure 5(a)). A weak reduction in the TEC can be seen at the similar MLAT
346 according to Figures 5(c) and (d). When the WID peak extends to 60 MLAT, it reaches the
347 plasmopause and drives the expansion of a plasmasphere finger (Figure 5(b)), a f. The orange
348 box in Figure 5(b) marks the period of finger development in the initial phase ($T = 705 \sim 750$ min
349 in Movie S1) and Figure 6 shows a snapshot of the finger-like structure that develops at the dusk
350 edge of the plasmopause and expands radially following the electric potential contour (marked
351 by the orange arrows) at 04:24 UT. We can see from Figure 6 that the cause of the plasmaspheric
352 finger is a result of the interaction between the plasmopause which is around $3.5 \sim 4R_E$ at the
353 early stage of the storm and the equatorward-expanding dusk convection cell of the electric field.

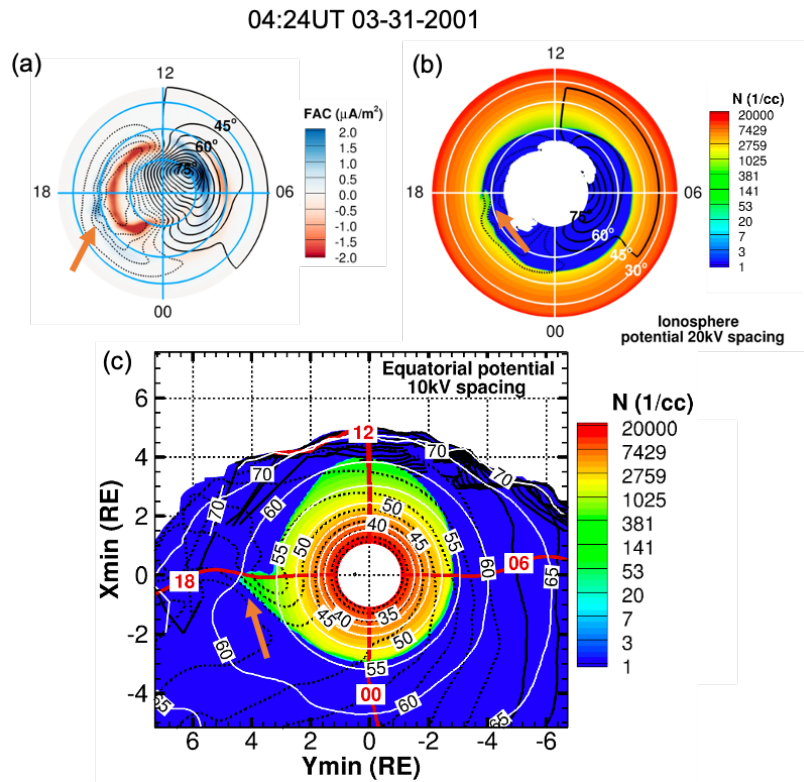


Figure 6. (a)-(c) Snapshots taken at 04:24UT 03-31-2001 at the end of the initial phase. (a) Simulated FAC in SM coordinates. (b) and (c) are ionospheric mapping and equatorial plane view of the plasmaspheric density with contour lines of the indicated MLT (red) and latitude (white) mapped to the plane. Black contour lines in (a-b) and (c) show electric potential with 20kV and 10kV intervals respectively, dashed for negative values. The orange arrows point to the location of the enhanced electric fields and the plasmasphere finger between 55 to 60 MLAT during the initial phase, which correspond to the westward drift velocity peak marked in Figure 5(a) by the box of the same color.

354

355 4.2.2 Erosion on the geospace plume

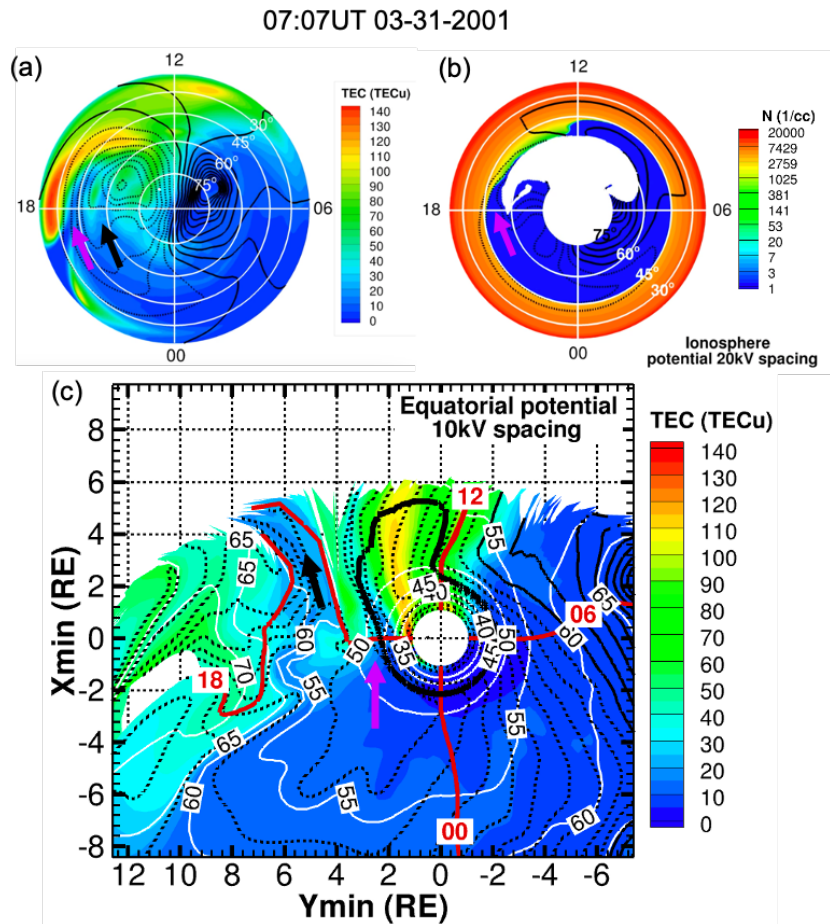


Figure 7. (a)-(c) Snapshots taken at 07:07UT 03-31-2001 in the late main phase. (a) Simulated TEC in SM coordinate. (b) and (c), same variables as in Figure 6. The purple and black arrows point to the locations of the density depletion, which correspond to the SAPS channel and the CRF marked in Figure 5 by the box of the same colors.

357 During the main phase (around 04:30~8:10UT, $T = 750\sim 970$ min in Movie S1), the two-
 358 cell convection pattern has established, double-band WID velocity peaks appear (Figure 5(a)),
 359 with one peak located at higher latitudes around 60 MLAT marked by the black box and another
 360 located at midlatitudes around 45~50 MLAT marked by the purple box. As shown in Figure
 361 5(b), the plasmapause in the purple box moves from 55 MLAT to 45 MLAT. The velocity peak
 362 around 60 MLAT does not overlap with the plasmasphere and thus, cannot directly interact with
 363 and influence it. In Figure 5(c), two large WID velocity channels are collocated with regions of
 364 low TEC, which can be seen in both black and purple boxes. The TEC depletion effect along
 365 with the midlatitude subauroral velocity peak is much more prominent according to Figure 5(d),
 366 where the depletion in TEC and ionospheric electron densities is quite obvious. However, ΔTEC
 367 in the black box does not show a negative value, which means the decrease of the TEC around
 368 60 MLAT may not be an obvious storm effect. Figure 7 shows the snapshots of TEC depletion
 369 and the plasmaspheric erosion corresponding to the double-band WID velocity channels (marked

370 by the black and purple arrows). Figure 7(c) demonstrates clearly that in the equatorial plane, the
371 midlatitude velocity peak (purple arrow) is collocated with TEC depletion and erodes the dusk
372 edge of the plasmaspheric plume, while the higher latitude velocity peak (black arrow) is only
373 coincident with a TEC depletion, since the plasmopause has been eroded to lower L-shell and
374 latitude.

375

376 4.2.2.1 Erosion on the plasmasphere

377

378 The double-peak feature in the WIDs is examined by Lin et al. (2021), who used the
379 MAGE model to perform a set of controlled numerical experiments and demonstrated that the
380 diffuse electron precipitation plays a crucial role in causing the latitudinal structure of the SAPS
381 electric field. Figures 8(a) - (d) show the sampled FAC, electron precipitation, ionospheric
382 conductance and electric field strength along 18 MLT at 07:07UT 03-31-2001. The green shade
383 marks the auroral region which consists of the diffuse electron precipitation and the mono-
384 energetic electron precipitation. The electron precipitation increases the local ionization rate in
385 the ionosphere E-region and enhances the Pedersen and Hall conductance. A portion of the
386 Region-2 current is located equatorward of the diffuse electron precipitation, where the
387 conductance is comparatively low. This leads to a strong poleward electrostatic field in the sub-
388 auroral region marked by the orange shade. The sub-auroral polarization stream (SAPS) is the
389 WID that is constrained between the low latitude boundary of the dusk-side diffuse electron
390 precipitation and the low latitude boundary of the dusk-side Region-2 current. The SAPS
391 velocity peaks around $45^{\circ}\sim 50^{\circ}$ and it overlaps with the plasmopause, causing a sunward ion flow
392 shown in Figure 8(f). The advection flow transports the cold plasma away from the plasmasphere
393 and to the dayside, which explains the erosion on the plasmopause marked by the purple box in
394 Figure 5(b). The velocity peak located at higher latitudes around 57° is inside the range of the
395 Region-1 current. It peaks in the region between the diffuse and the mono-energetic precipitation
396 where the conductance is also comparatively low and the closure of Region-1 and the Region-2
397 currents results in a strong electric field. This electric field causes WID velocity peak and we call
398 it the convection return flow (CRF). The CRF does not interact with the plasmasphere, which is
399 consistent with Figure 5(b).

400

401 4.2.2.1 Depletion of the TEC

402

403 Figure 8(g) shows the MLAT profile of TEC, where there are two electron density/TEC
404 troughs with one co-located with the peak of CRF around 55 MLAT and the other located around
405 42 MLAT, to the equatorward of the SAPS peak. The factors that contribute to the depletion of
406 the ionospheric TEC are much more complicated than the plasmaspheric erosion. The formation
407 of the electron density trough is discussed by Lu et al. (2020), where they examined the rate of
408 change for O^+ density in the TIEGCM, which is considered as a proxy for the electron content. In
409 general, the rate of change is determined by the O^+ production and loss rate, ambipolar diffusion,
410 neutral wind transport, and the $\mathbf{E}\times\mathbf{B}$ transport. Lu et al. gave a detailed analysis of the
411 contribution from each process. They showed that the $\mathbf{E}\times\mathbf{B}$ transport is the major contributor to
412 the formation of the sub-auroral electron density trough. This transport brings the low electron
413 density into the high-density region, and this depletion is further enhanced with the increased
414 loss/recombination rate of the ions at a higher temperature caused by the significantly enhanced
415 frictional heating due to the strong ion drifts in the WID channel (Schunk et al., 1976). The

416 analysis above is consistent with our results. However, the equatorward shift of the midlatitude
 417 electron density trough in Figure 8(g) indicates other transport effects and needs further
 418 investigation in the future.
 419

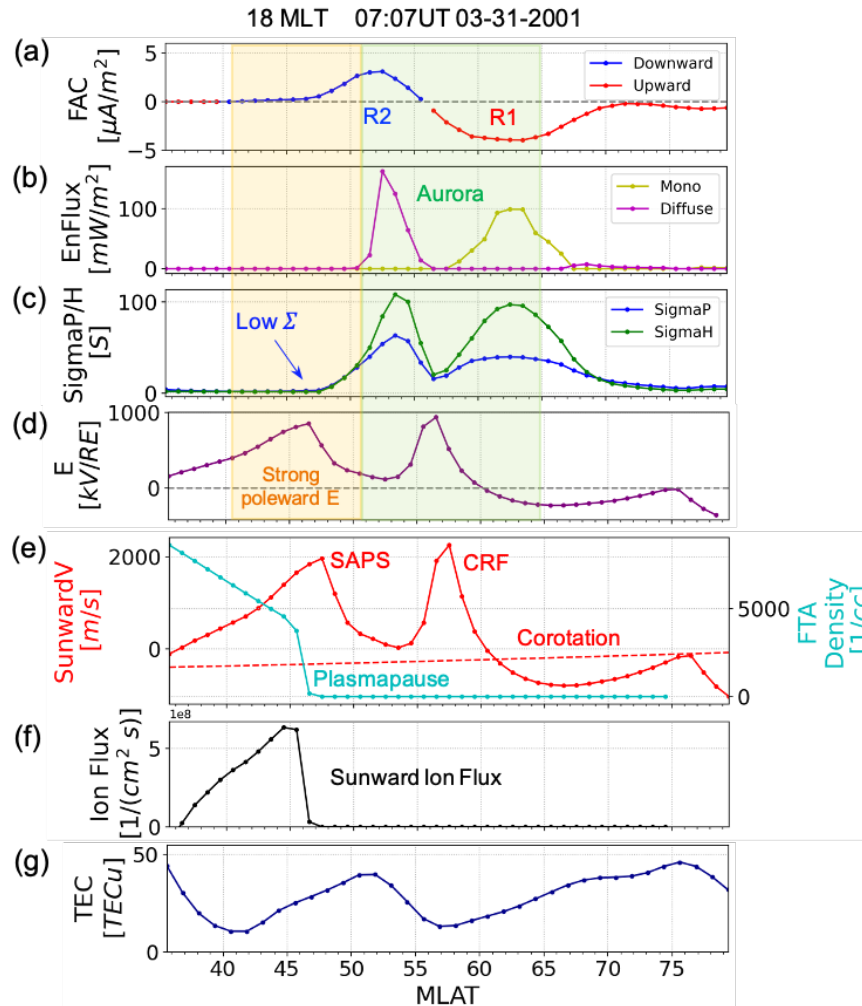


Figure 8. (a)-(e) Latitudinal profiles of REMIX ionospheric quantities sampled at 18 MLT and 07:07UT. (a) Upward Region-1 (red) and downward Region-2 current (blue). (b) Energy flux of diffuse (magenta) and mono-energetic (olive) electron precipitation. (c) Pedersen conductance (blue) and Hall conductance (green). (d) Electric field strength. (e) Calculated $E \times B$ ion drift velocity (red) with corotation velocity shown by the dashed line. The cyan curve is the flux-tube-averaged (FTA) plasmaspheric density mapped to the ionospheric grid. (f) Calculated sunward ion flux based on density and ion drift velocity in (e). (g) Total electron content.

421 4.2.2.1 Data-model comparison on the erosion effect

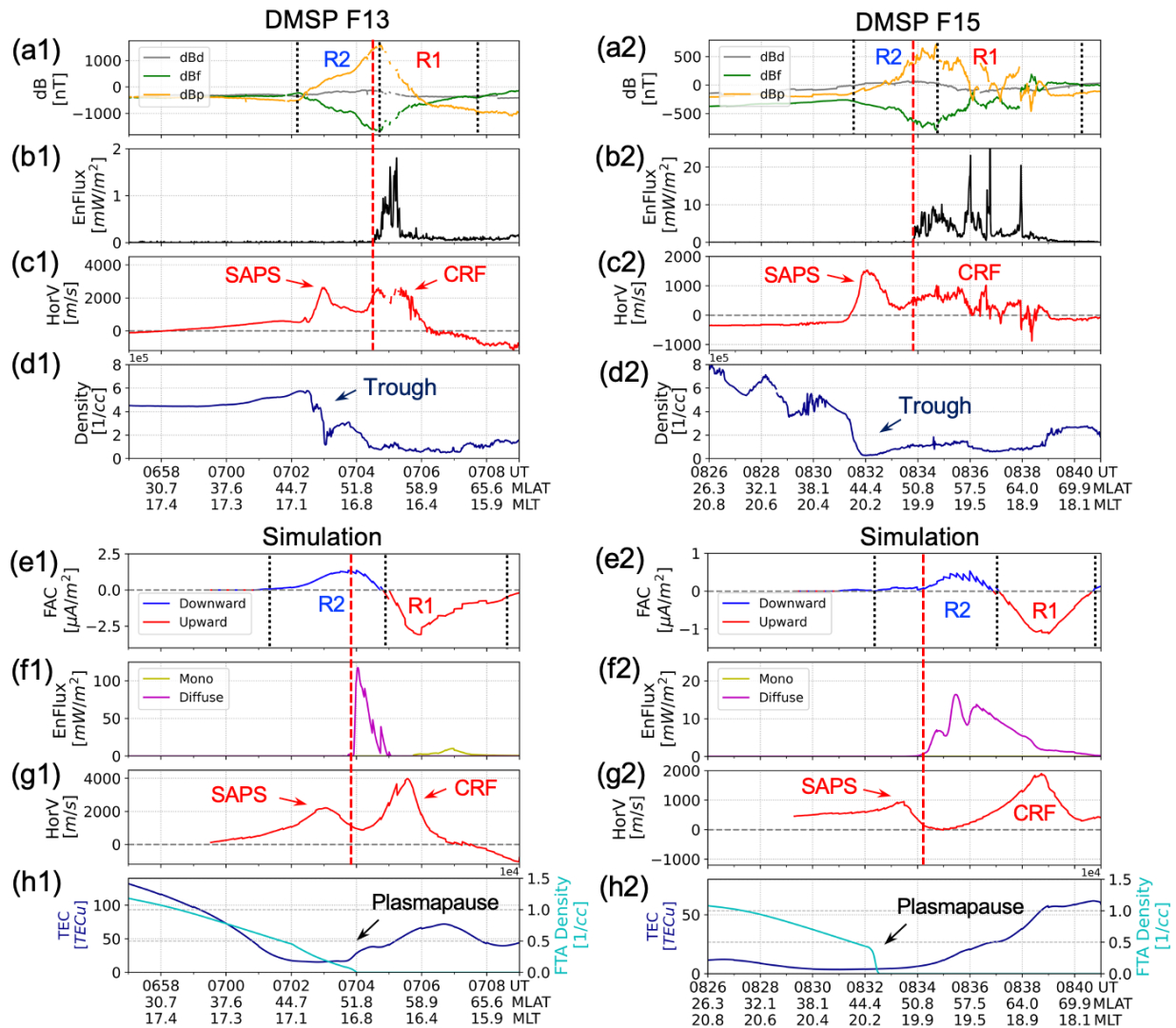


Figure 9. DMSP F13 and F15 (~850km in altitude) measurements at 06:57 ~ 07:09UT, March 31, 2001: **(a1)-(a2)** magnetic perturbation in the downward (dBd), forward (dBf) and perpendicular (horizontal cross-track) (dBp) direction relative to the satellite track direction; **(b1)-(b2)** precipitating electron energy flux; **(c1)-(c2)** horizontal cross-track sunward ion drift velocity; and **(d1)-(d2)** electron density. The dashed black lines in **(a1)-(a2)** divide the range of the Region-1 and the Region-2 currents based on the slopes of the magnetic perturbation curves. The dashed red line is the equatorward auroral boundary. Simulated quantities sampled along the satellite track: **(e1)-(e2)** field-aligned current; **(f1)-(f2)** energy flux of diffuse electron precipitation (magenta) and mono-energetic precipitation (olive); **(g1)-(g2)** simulated ion drift velocity in the DMSP horizontal cross-track sunward direction; **(h1)-(h2)** simulated electron density (navy) and flux-tube-averaged plasmaspheric density (black).

422

423

424

Sections 4.2.2.1 and 4.2.2.2 discuss the double-peak feature in WIDs on the dusk side and their effect on the plasmaspheric erosion and ionospheric TEC depletion. In this section, we

425 investigate this subject with DMSP observations. Figure 9 shows a data-model comparison of the
426 FAC, the ionospheric differential number flux of the electron precipitation, the horizontal ion
427 drift velocity, and the electron density. Figures 9(a1) - (d1) and (a2) - (d2) are DMSP F13 and
428 F15 measurements during 06:57 ~ 07:09UT and 08:26 ~ 08:41UT, 03-31-2001 respectively.
429 Ranges of the Region-1 and the Region-2 currents can be derived from the magnetic field
430 perturbation following the method from J. Liu et al. (2022), which are divided by the back
431 dashed line in Figures 9(a1) and (a2). Figures 9(e1) - (h1) and (e2) - (h2) are the corresponding
432 physical quantities from the MAGE simulation along the satellite trajectories. Since the satellites
433 usually fly beyond the altitude range of TIEGCM, we plot the TEC and the plasmaspheric flux-
434 tube-averaged (FTA) density instead. The dashed red line is the equatorward auroral boundary
435 using the same criteria as in Figure 8.

436
437 Figures 9(a1) - (d1) and (a2) - (d2) show that dusk-side electron precipitation is located
438 mostly within the range of the Region-1 current with a slight overlap on the Region-2 current.
439 The SAPS is located in the sub-auroral region within the range of the Region-2 current. The CRF
440 covers the region between the Region-1 and Region-2 current and some portion of the Region-1
441 current. The spikes in the electron precipitation, e.g., around 55 MLAT at 07:05UT correspond
442 to the dips in the CRF velocity. The large velocity of SAPS (Figure 9(c1)) is collocated with an
443 acute trough in the ionospheric electron density. The electron density is also low at higher
444 latitudes, corresponding to the location of CRF. This is consistent with the result shown in Figure
445 8.

446
447 Compared with the DMSP data, the simulation predicts similar location of the Region-1/2
448 currents and electron precipitation. The model overestimates the strength of the precipitation
449 energy flux in Figure 9(f1), but according to the following REMIX output it is transient and it
450 does not impact the ionospheric conductance much. In terms of the WID velocity, the double-
451 band feature of WIDs, SAPS and CRF peaks, are successfully reproduced. The SAPS velocity is
452 around 2000 m/s at 07:03UT and 1000m/s at 08:33UT, which are in reasonable agreement with
453 the observations.

454
455 In Figures 9(h1) and (h2), the location of the plasmopause and the TEC depletion can be
456 seen and compared with the observations. The simulated TEC troughs corresponding to SAPS
457 are much broader than the electron density troughs in the observation. The FTA plasmaspheric
458 density, on the other hand, has good agreement with the observations of the electron density in
459 Figures 9(d1) and (d2): At 07:03UT (near 48 MLAT, 17 MLT), in the observation (Figure 9(d1)),
460 the SAPS velocity peak still overlaps with the region with substantial electron content and
461 causing a density trough to mirror the SAPS peak. In the simulation (Figure 9(h1)), the SAPS
462 peak also overlaps with a portion of the plasmasphere which causes sunward plasmaspheric
463 particle transport. In the later satellite pass at 08:32UT (near 46 MLAT, 20 MLT) as shown in
464 Figure 9(d2), the SAPS velocity peak corresponds to a substantially depleted electron density
465 that forms a distinct boundary in the density profile. In the simulation (Figure 9(h2)), the same
466 sharp drop in the FTA density is captured by the model. Combined with the analysis of the
467 sunward ion flux caused by SAPS at the plasmopause in Figure 8(e)-(f), this data-model
468 comparison confirms the effect of SAPS in depleting the local plasma content.
469

470 In Section 4.2, we have discussed the formation of the WIDs and investigated their role
471 in depleting the local plasma density. During storm main phase, in both simulation and
472 observation, two velocity peaks can be found in the WIDs. The one at the midlatitude is the
473 SAPS channel. The transportation effect of SAPS causes the erosion of the plasmopause at its
474 dusk side and the TEC depletion in the trough region. In the next section, we further investigate
475 the factors that determine the spatial distribution of Region-2 current and the electron
476 precipitation that lead to the SAPS electric field and their relation to the geospace plume
477 evolution.

478 479 4.3 Relationship between ring current build-up and geospace plume development 480

481 As discussed in Section 4.2, the Region-2 current and electron precipitation directly
482 control the SAPS electric field development in the ionosphere. In this section, we further explore
483 the major factors in the magnetosphere that drive SAPS development and the geospace plume
484 evolution from the perspective of M-I coupling.
485

486 Figures 10(a) and Figure 11(a) show contours of the specified values in the plasma profile
487 as a marker of the plasmopause (black), the ring current ion pressure (red), the electron pressure
488 (green), the equatorial mapping of the energy flux of diffuse electron precipitation (orange), the
489 FAC (background) and the electrostatic potential (light solid and dashed contours) at the
490 beginning (04:48UT) and the end (07:41UT) of the storm main phase. The variable values
491 enclosed by the colored contour lines are larger than the contour values. The contour values are
492 chosen to best describe the spatial distribution of the variables (see Figure S1). The red arrows
493 point to the critical region, where the dusk-side Region-2 current (in blue) is located. At the
494 sunward azimuthal edge of the ring current ion pressure (represented by the magenta contour),
495 the large pressure gradient distorts the magnetic field lines and generates the Region-2 current
496 that connects to the partial ring current and flows into the ionosphere. The magnetospheric
497 source region of diffuse precipitation is located in the region with high electron pressure and it
498 partially overlaps with the Region-2 current. This results in a strong SAPS electric field co-
499 located with the low-latitude portion of the Region-2 current where there is little electron
500 precipitation. This result is consistent with previous MAGE modeling work of SAPS (Lin et al.,
501 2021) and earlier works describing the basic physics of SAPS (e.g., Foster & Vo, 2002).
502

503 During the period of geospace plume erosion by SAPS (from Figure 11(a) to Figure
504 11(a)), the high electron pressure region, which is the source region of the electron precipitation,
505 is always located at the outer boundary of the ring current ion pressure 100 nPa contour. As a
506 result, the electron precipitation always covers a portion of the Region-2 current which maintains
507 the persistent SAPS electric field located at the inner boundary of the ring current contour and
508 the dusk edge of the plasmopause. The strong SAPS electric field dominates the spatial
509 distribution of the electric potential and evolves the plasmaspheric plume into the dusk side. The
510 joint evolution of the ring current and the plasmasphere is shown in Movie S3 and a similar
511 spatial relation of the two is observed by the IMAGE satellite (Figure S2).
512

513 We now ask, what determines the spatial distributions of the ring current electron and ion
514 pressure that impact the source regions of diffuse electron precipitation and the Region-2
515 currents? The cold plasmaspheric protons are subject to the $\mathbf{E} \times \mathbf{B}$ drift and corotation. Besides

516 these two drifts, the hot protons and electrons, after being transported to the inner
 517 magnetosphere, are also subjected to gradient/curvature drift in opposite directions. In RCM, the
 518 total drift effect is represented by the effective potential defined by adding the term $V^{-2/3}$.
 519 $\lambda_{i,k}/e$ to the equatorial electric potential (Toffoletto et al., 2003). This effective electric potential
 520 for species i at energy channel k is given by

$$521 \quad \phi_{eff,k,i} = \phi_I + \lambda_{i,k} \cdot V^{-2/3}/e + \phi_c \quad (3)$$

522 where $\lambda_{i,k}$ is the energy invariant for species i at channel k in RCM and the closed magnetic flux
 523 tube volume V is given by

$$524 \quad V = \int \frac{ds}{B_{MHD}} \quad (4)$$

525
 526 Figures 10, 11(b) - (d) show the flux tube content (η) in the magnetic flux tube from the
 527 RCM characteristic energy channels of the plasmasphere ($\lambda_0 = 0$), hot protons and hot electrons
 528 at the beginning and the end of the storm main phase. The proton and the electron channels
 529 shown ($\lambda_p = 1639.46$, $\lambda_e = -234.21$, in RCM units, $eV \cdot (R_E/nT)^{2/3}$) are the ones that contribute
 530 most to the total proton pressure and the total electron pressure (as well as the diffuse
 531 precipitation energy flux) respectively. The corresponding energy of the proton and the electron
 532 at the selected channels is around 80 keV and 8 keV at the location of the ring current and the
 533 electron precipitation. The effective potential of the channel is plotted as black contour lines with
 534 dashed lines for negative values.

535
 536 Comparing the effective electric potential contours in Figures 10 (b) - (d), we can see the
 537 gradient and curvature term in the proton effective electric field (*Potential_P*) dominates the
 538 inner magnetosphere and is a result of the comparatively large energy invariant of that proton
 539 channel. The electron effective electric potential (*Potential_E*) contours look similar to the
 540 plasmaspheric electric potential (*Potential_0*) especially outside the geosynchronous orbit,
 541 since the gradient and curvature term for electrons is comparatively weak due to their lower
 542 particle energy. During the early main phase, the ring current particles have just been transported
 543 by the convection electric field to the inner magnetosphere and started to drift following their
 544 effective electric potential contours. Meanwhile, the plasmaspheric plume expands sunward
 545 driven by the convection electric field. At this moment, the η distributions of the plasmasphere,
 546 proton and electron are approximately symmetric about the x-axis ($Y = 0$) and the conditions for
 547 the SAPS formation have just started to appear on the dusk edge of the plasmasphere.

548
 549 At the late main phase, as shown in Figure 11(c), the η distribution shows that the ring
 550 current hot protons have drifted westward from the nightside and penetrated deep inside $2R_E$ on
 551 the dayside (marked by the yellow arrow). The Region-2 current originating at the outer edge of
 552 the partial ring current beyond $2R_E$ has shifted toward the dayside accordingly (in Figure 11(a)).
 553 The SAPS electric field have been very strong and dominated the geometry of *Potential_0* and
 554 *Potential_E*. On one hand, it causes the plasmaspheric plume to move to the dusk side. On the
 555 other hand, the hot electrons (in Figure 11(d)) are obstructed by the strong dusk-side electric
 556 fields with major contribution from SAPS. The electrons accumulate outside the SAPS flow
 557 channel around $3R_E$ and form a sharp edge in the electron η distribution (marked by the orange
 558 arrow). This leads to a distinct equatorward edge of the ionospheric diffuse precipitation and the

559 absence of electron precipitation in part of the Region-2 current that helps to maintain the strong
 560 SAPS electric field.
 561

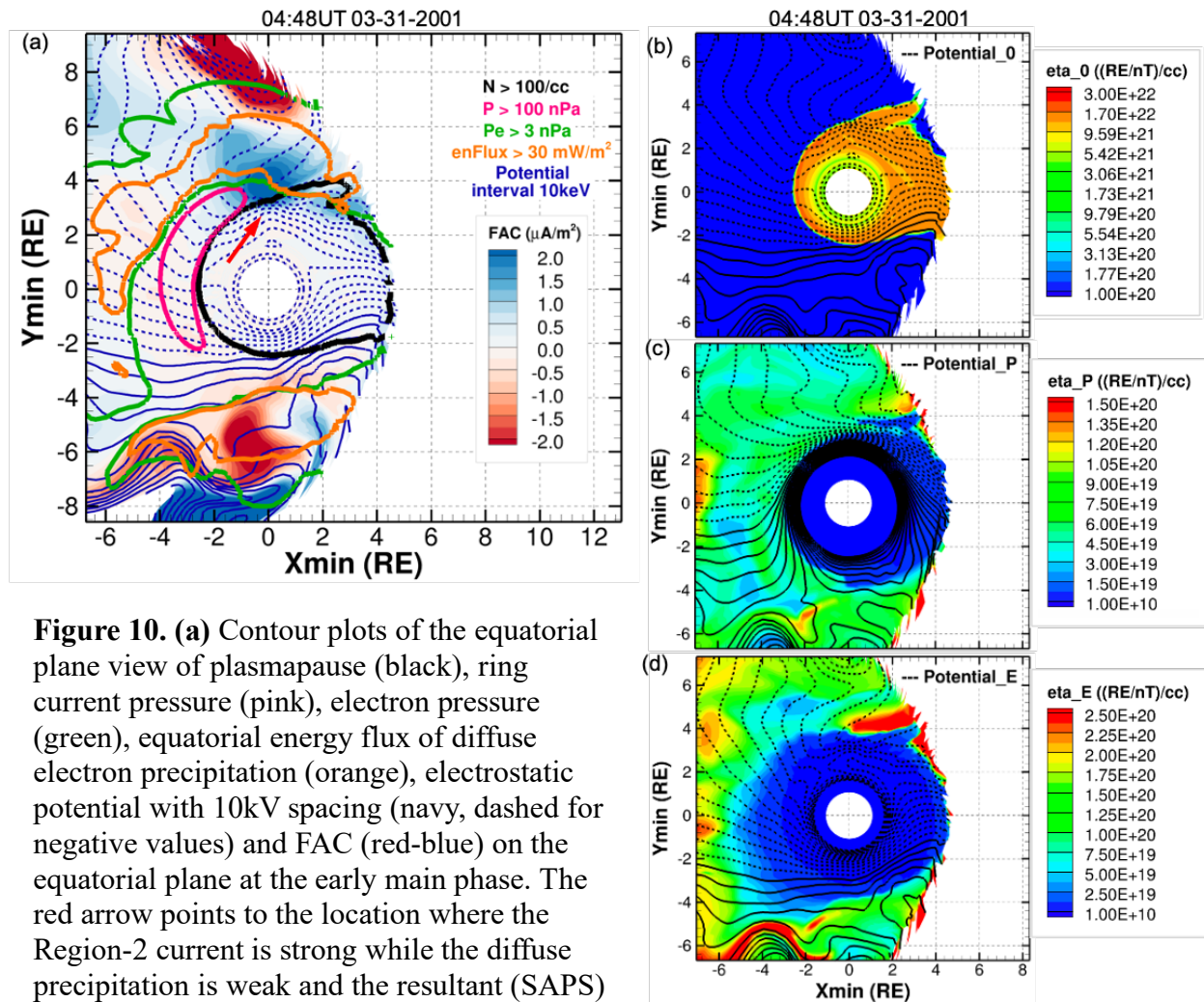


Figure 10. (a) Contour plots of the equatorial plane view of plasmapause (black), ring current pressure (pink), electron pressure (green), equatorial energy flux of diffuse electron precipitation (orange), electrostatic potential with 10kV spacing (navy, dashed for negative values) and FAC (red-blue) on the equatorial plane at the early main phase. The red arrow points to the location where the Region-2 current is strong while the diffuse precipitation is weak and the resultant (SAPS) electrostatic field is intense. (b)-(d) Contour plots of the RCM η variable for the plasmaspheric energy channel, the proton energy channel that contributes most to the ring current pressure and the electron energy channel that contributes most to the electron pressure/diffuse precipitation energy flux and their corresponding effective electric potential on the equatorial plane.

562
 563 The analysis above demonstrates that the storm-time energy-dependent electron and
 564 proton drifts determine the spatial distribution of Region-2 currents and diffuse electron
 565 precipitation. The ring current ion can overcome the existing SAPS electric field and penetrate
 566 into deeper L-shell at dayside, while the ring current electrons cannot due to their featured

567 adiabatic invariants of their drifts. This delicate balance between the energy-dependent
 568 gradient/curvature drift and the $\mathbf{E} \times \mathbf{B}$ drifts self-consistently maintains the SAPS electric field to
 569 further erode the dusk-side plasmasphere and push the plasmaspheric plume shifting toward the
 570 dusk side.

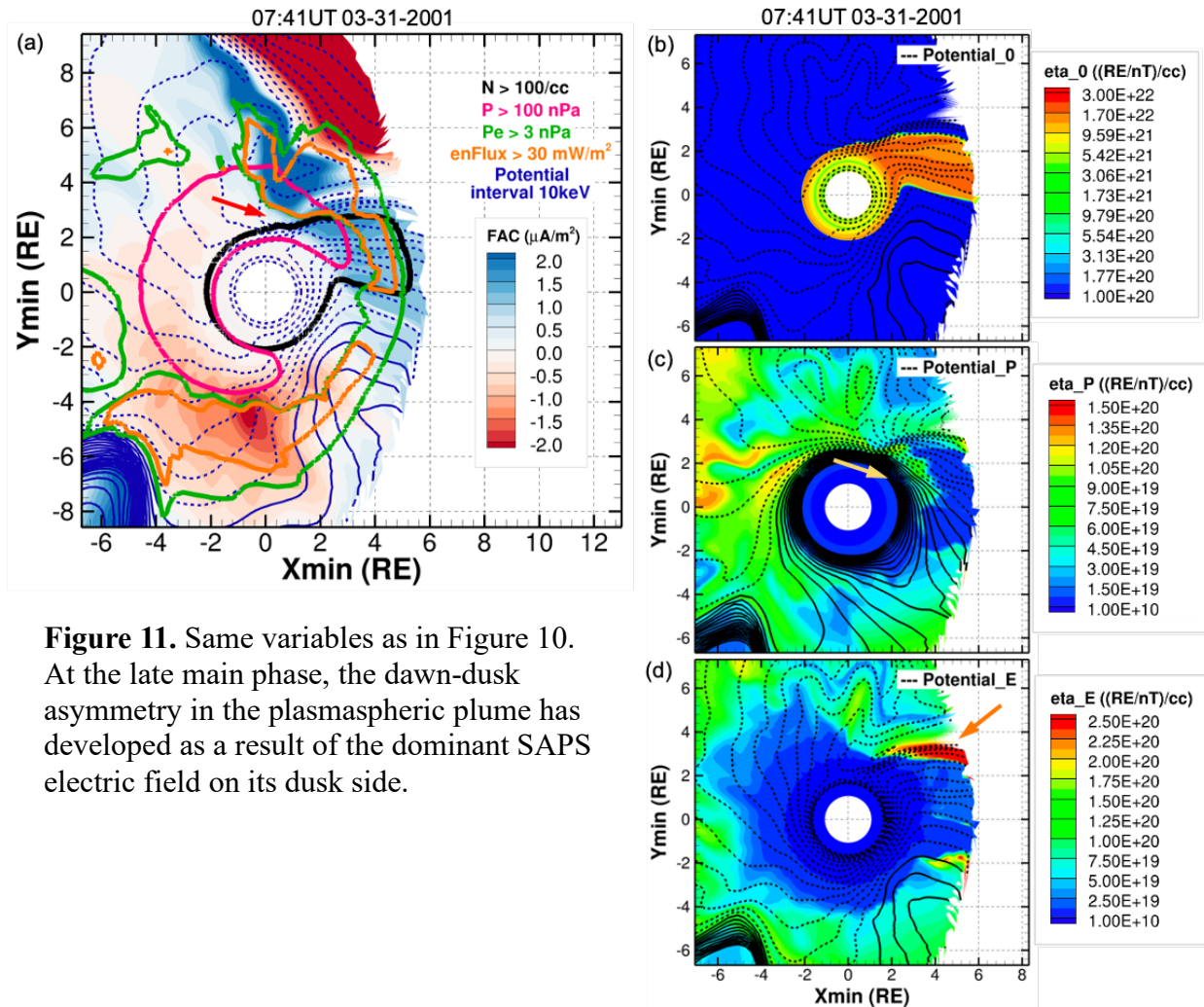


Figure 11. Same variables as in Figure 10. At the late main phase, the dawn-dusk asymmetry in the plasmaspheric plume has developed as a result of the dominant SAPS electric field on its dusk side.

571 572 4.5 Model limitations

573
 574 The MAGE simulation of the March 31, 2001 storm presented above demonstrates
 575 clearly the close relation between the global-scale convection, ring current build-up, FAC, and
 576 electron precipitation which dynamically alter the geospace plume system. However, there are
 577 some limitations. First, the model did not include the plasma transport between the plasmasphere
 578 and the ionosphere. Although, as discussed in Section 1.2.2.2, plasmaspheric refilling is much
 579 slower compared with the dynamic transport of the plasma within the plasmasphere and
 580 ionosphere during the storm main phase (Lawrence et al., 1999; Denton et al., 2012; Krall et al.,
 581 2014), plasma exchange between the plasmasphere and ionosphere can be important in the storm
 582 recovery phase (Carpenter & Lemaire, 1997). Second, as discussed in Section 4.3, during the
 583 later stage of the storm main phase, the simulated ring current overlaps with the plasmasphere,
 584 especially in the plume region. In this work, our model did not include ring current ion loss due

585 to the EMIC wave scattering (Erlandson & Ukhorskiy, 2001; Goldstein et al., 2003), although it
586 is possible that ion precipitation may affect the ionospheric conductance and feed back to the
587 magnetospheric system (Tian et al., 2022). Furthermore, inside the plasmasphere, the energetic
588 electrons resonate with hiss waves and contribute to diffuse electron precipitation (Ma et al.,
589 2021). The current version of the model did not take into account such wave-particle
590 interactions. We are working on including these important precipitation mechanisms to better
591 inform the ring current particle loss and ionospheric precipitation in future versions of the model
592 (Bao et al., 2022; Lin et al., 2022).
593

594 **4 Summary and Conclusions**

595 In this paper, we investigate the evolution of the geospace plume during the March 31,
596 2001 superstorm using the MAGE model, which coupled the global and inner magnetosphere,
597 the ionosphere and the thermosphere. Combined with satellite observations, we used the MAGE
598 simulation to address the three major science questions raised in the introduction section.
599

600 The first question is the cause of the linkage and joint evolution of the two counterparts
601 of the geospace plume, the plasmaspheric plume and the ionospheric SED plume. We conclude
602 that the $\mathbf{E} \times \mathbf{B}$ transport of the plasma by the coupled magnetosphere-ionosphere electric field is
603 the major process that causes the plasmaspheric plume and the ionospheric SED plume to evolve
604 in a similar way and to have co-located footprints on the equatorial plane.
605

606 The second and third science questions are closely tied together. The second science
607 question focuses on identifying the specific processes that are important for shaping the
608 plasmasphere and the ionosphere plume. The third science question explores the relationship
609 between the build-up of the ring current and the development of the geospace plume. The
610 simulation shows that geospace plume in the equatorial plane expands sunward due to the
611 convection electric field in the early main phase. The plume shifts toward the dusk side in the
612 late main phase. We also find two channels of TEC depletion, with one in the ionosphere
613 midlatitude trough region, corresponding to the dusk edge of the plasmasphere, and the other at
614 higher latitudes inside the auroral oval. By investigating the related physical quantities along 18
615 MLT and comparing with DMSP observations, we find that the westward SAPS flow is the
616 major cause of the erosion on the dusk edge of the plasmasphere and duskward shift of the
617 geospace plume, which answers science question two. We further investigate the cause of the
618 spatial distributions of the Region-2 currents and diffuse precipitation that are responsible for the
619 occurrence of SAPS by analyzing the effective electric fields of ring current protons and
620 electrons. Region-2 current is located at the sunward boundary of the ring current mostly
621 contributed by hot protons, where the pressure gradient distorts the magnetic field. Due to the
622 energy-dependent charged particle drifts, the ring current pressure is located preferentially on the
623 dusk side. The region of energetic ring current electrons, as the source region of the diffuse
624 precipitation, are at larger L-shells compared to the region of high ion pressure. As a result, the
625 SAPS electric field is generated at the location where a part of the Region-2 current does not
626 overlap with the diffuse precipitation and the ionospheric conductance is low. The analysis of the
627 RCM energy channels shows the ring current ions can overcome the existing SAPS electric field
628 and penetrate into deeper L-shell at dayside, while the ring current electrons cannot due to their
629 featured adiabatic invariants of their drifts. This delicate balance between the energy-dependent

630 gradient/curvature drift and the $\mathbf{E} \times \mathbf{B}$ drifts self-consistently maintains the SAPS electric field.
631 We conclude that the intrinsic cause of the SAPS and the resulting plasmasphere erosion as well
632 as the plume geometry is the energy-dependent drifts of the ring current electrons and ions that
633 impact the coupled geospace system.
634

635 **Acknowledgments**

636 This work is supported by NASA DRIVE Science Center for Geospace Storms (CGS) grant
637 80NSSC22M0163, NASA O2R grant 80NSSC19K0241, NASA GCR grant 80NSSC17K0013 and
638 LWS grant 80NSSC20K0356. Dr. Viacheslav Merkin gratefully acknowledges support from
639 NASA LWS grants 80NSSC19K0080 and 80NSSC19K0071. We would like to acknowledge the
640 use of computational resources (doi:10.5065/D6RX99HX) at the NCAR-Wyoming
641 Supercomputing Center provided by the National Science Foundation and the State of Wyoming,
642 and supported by NCAR's Computational and Information Systems Laboratory. Dr. Shanshan
643 Bao thanks Dr. Joe Huba and Dr. Roger Varney for the valuable discussion on the modeling
644 work. The OMNI data are obtained from <https://cdaweb.gsfc.nasa.gov/index.html/>; the World-
645 wide TEC data and the DMSP data are provided by the CEDAR Madrigal Database
646 (<http://cedar.openmadrigal.org/index.html>); the simulation data selected for figures in this paper
647 are stored and published on Zenodo (via: <https://zenodo.org/record/7843840>).

648 **References**

- 649 Bao, S. (2019). Large-scale Coupled Models of the Inner Magnetosphere. Diss., Rice University.
650 Retrieved from <https://hdl.handle.net/1911/107801>.
- 651 Bao, S., Toffoletto, F., Yang, J., Sazykin, S., & Wiltberger, M. (2021). Coupling the Rice
652 Convection Model-Equilibrium to the Lyon-Fedder-Mobarry Global
653 Magnetohydrodynamic Model. *Journal of Geophysical Research: Space Physics*, 126(8).
654 <https://doi.org/10.1029/2020JA028973>
- 655 Bao, S., Lin, D., Sorathia, K., Wang, D., Toffoletto, F., Merkin, V., et al. (2022). Wave-
656 dependent ring current electron loss and magnetospheric precipitation during a geospace
657 storm. *AGU Fall Meeting Abstracts, 2022*, SM22F-1988.
- 658 Burch, J. L., Mitchell, D. G., Sandel, B. R., Brandt, P. C., & Wüest, M. (2001). Global dynamics
659 of the plasmasphere and ring current during magnetic storms. *Geophysical Research*
660 *Letters*, 28(6), 1159–1162. <https://doi.org/10.1029/2000GL012413>

- 661 Carpenter, D. L., & Lemaire, J. (1997). Erosion and recovery of the plasmasphere in the
662 plasmopause region. *Space Science Reviews*, 80(1/2), 153–179.
663 <https://doi.org/10.1023/A:1004981919827>
- 664 Cramer, W. D., Raeder, J., Toffoletto, F. R., Gilson, M., & Hu, B. (2017). Plasma sheet
665 injections into the inner magnetosphere: Two-way coupled OpenGGCM-RCM model
666 results. *Journal of Geophysical Research: Space Physics*, 122(5), 5077–5091.
667 <https://doi.org/10.1002/2017JA024104>
- 668 De Zeeuw, D. L., Sazykin, S., Wolf, R., Gombosi, T., Ridley, A., & Toth. (2004). Coupling of a
669 global MHD code and an inner magnetospheric model: Initial results. *Journal of*
670 *Geophysical Research*, 109(A12), A12219. <https://doi.org/10.1029/2003JA010366>
- 671 Denton, R. E., Wang, Y., Webb, P. A., Tengdin, P. M., Goldstein, J., Redfern, J. A., & Reinisch,
672 B. W. (2012). Magnetospheric electron density long-term (>1 day) refilling rates inferred
673 from passive radio emissions measured by IMAGE RPI during geomagnetically quiet
674 times: MAGNETOSPHERIC ELECTRON DENSITY REFILLING RATES. *Journal of*
675 *Geophysical Research: Space Physics*, 117(A3), n/a-n/a.
676 <https://doi.org/10.1029/2011JA017274>
- 677 Erlandson, R. E., & Ukhorskiy, A. J. (2001). Observations of electromagnetic ion cyclotron
678 waves during geomagnetic storms: Wave occurrence and pitch angle scattering. *Journal*
679 *of Geophysical Research: Space Physics*, 106(A3), 3883–3895.
680 <https://doi.org/10.1029/2000JA000083>
- 681 Fagundes, P. R., Cardoso, F. A., Fejer, B. G., Venkatesh, K., Ribeiro, B. A. G., & Pillat, V. G.
682 (2016). Positive and negative GPS-TEC ionospheric storm effects during the extreme
683 space weather event of March 2015 over the Brazilian sector: POSITIVE AND

- 684 NEGATIVE IONOSPHERIC STORM. *Journal of Geophysical Research: Space Physics*,
685 121(6), 5613–5625. <https://doi.org/10.1002/2015JA022214>
- 686 Foster, J. C., & Burke, W. J. (2002). SAPS: A new categorization for sub-auroral electric fields.
687 *Eos, Transactions American Geophysical Union*, 83(36), 393.
688 <https://doi.org/10.1029/2002EO000289>
- 689 Foster, J. C., & Vo, H. B. (2002). Average characteristics and activity dependence of the
690 subauroral polarization stream: SUBAURORAL POLARIZATION STREAM. *Journal of*
691 *Geophysical Research: Space Physics*, 107(A12), SIA 16-1-SIA 16-10.
692 <https://doi.org/10.1029/2002JA009409>
- 693 Foster, J. C., Erickson, P. J., Coster, A. J., Goldstein, J., & Rich, F. J. (2002). Ionospheric
694 signatures of plasmaspheric tails. *Geophysical Research Letters*, 29(13), 1623.
695 <https://doi.org/10.1029/2002GL015067>
- 696 Foster, J. C., Erickson, P. J., Coster, A. J., Thaller, S., Tao, J., Wygant, J. R., & Bonnell, J. W.
697 (2014). Storm time observations of plasmasphere erosion flux in the magnetosphere and
698 ionosphere: Foster et al.: Plasmasphere Erosion Flux. *Geophysical Research Letters*,
699 41(3), 762–768. <https://doi.org/10.1002/2013GL059124>
- 700 Foster, J. C., Erickson, P. J., Walsh, B. M., Wygant, J. R., Coster, A. J., & Zhang, Q. (2020).
701 Multi-Point Observations of the Geospace Plume. In Q. Zong, P. Escoubet, D. Sibeck, G.
702 Le, & H. Zhang (Eds.), *Geophysical Monograph Series* (1st ed., pp. 243–264). Wiley.
703 <https://doi.org/10.1002/9781119509592.ch14>
- 704 Foster, J.C., Rideout, W., Sandel, B., Forrester, W. T., & Rich, F. J. (2007). On the relationship
705 of SAPS to storm-enhanced density. *Journal of Atmospheric and Solar-Terrestrial*
706 *Physics*, 69(3), 303–313. <https://doi.org/10.1016/j.jastp.2006.07.021>

- 707 Foster, John C. (1993). Storm time plasma transport at middle and high latitudes. *Journal of*
708 *Geophysical Research: Space Physics*, *98*(A2), 1675–1689.
709 <https://doi.org/10.1029/92JA02032>
- 710 Gallagher, D. L., Craven, P. D., & Comfort, R. H. (2000). Global core plasma model. *Journal of*
711 *Geophysical Research: Space Physics*, *105*(A8), 18819–18833.
712 <https://doi.org/10.1029/1999JA000241>
- 713 Goldstein, J. (2004). Simultaneous remote sensing and in situ observations of plasmaspheric
714 drainage plumes. *Journal of Geophysical Research*, *109*(A3), A03202.
715 <https://doi.org/10.1029/2003JA010281>
- 716 Goldstein, J. (2007). Plasmasphere Response: Tutorial and Review of Recent Imaging Results.
717 *Space Science Reviews*, *124*(1–4), 203–216. <https://doi.org/10.1007/s11214-006-9105-y>
- 718 Goldstein, J., & Sandel, B. R. (2005). The global pattern of evolution of plasmaspheric drainage
719 plumes. In J. Burch, M. Schulz, & H. Spence (Eds.), *Geophysical Monograph Series*
720 (Vol. 159, pp. 1–22). Washington, D. C.: American Geophysical Union.
721 <https://doi.org/10.1029/159GM02>
- 722 Goldstein, J., Sandel, B. R., Hairston, M. R., & Reiff, P. H. (2003). Control of plasmaspheric
723 dynamics by both convection and sub-auroral polarization stream: PLASMASPHERIC
724 DYNAMICS. *Geophysical Research Letters*, *30*(24).
725 <https://doi.org/10.1029/2003GL018390>
- 726 Goldstein, J., Burch, J. L., & Sandel, B. R. (2005). Magnetospheric model of subauroral
727 polarization stream: MAGNETOSPHERIC SAPS MODEL. *Journal of Geophysical*
728 *Research: Space Physics*, *110*(A9). <https://doi.org/10.1029/2005JA011135>

- 729 Goldstein, J., Thomsen, M. F., & DeJong, A. (2014). In situ signatures of residual plasmaspheric
730 plumes: Observations and simulation. *Journal of Geophysical Research: Space Physics*,
731 *119*(6), 4706–4722. <https://doi.org/10.1002/2014JA019953>
- 732 Huba, J., & Krall, J. (2013). Modeling the plasmasphere with SAMI3: MODELING THE
733 PLASMASPHERE WITH SAMI3. *Geophysical Research Letters*, *40*(1), 6–10.
734 <https://doi.org/10.1029/2012GL054300>
- 735 Huba, J. D., & Sazykin, S. (2014). Storm time ionosphere and plasmasphere structuring: SAMI3-
736 RCM simulation of the 31 March 2001 geomagnetic storm. *Geophysical Research*
737 *Letters*, *41*(23), 8208–8214. <https://doi.org/10.1002/2014GL062110>
- 738 Huba, J. D., Sazykin, S., & Coster, A. (2017). SAMI3-RCM simulation of the 17 March 2015
739 geomagnetic storm. *Journal of Geophysical Research: Space Physics*, *122*(1), 1246–
740 1257. <https://doi.org/10.1002/2016JA023341>
- 741 Krall, J., Huba, J. D., Denton, R. E., Crowley, G., & Wu, T.-W. (2014). The effect of the
742 thermosphere on quiet time plasmasphere morphology. *Journal of Geophysical Research:*
743 *Space Physics*, *119*(6), 5032–5048. <https://doi.org/10.1002/2014JA019850>
- 744 Lawrence, D. J., Thomsen, M. F., Borovsky, J. E., & McComas, D. J. (1999). Measurements of
745 early and late time plasmasphere refilling as observed from geosynchronous orbit.
746 *Journal of Geophysical Research: Space Physics*, *104*(A7), 14691–14704.
747 <https://doi.org/10.1029/1998JA900087>
- 748 Lemaire, J. F., Gringauz, K. I., Carpenter, D. L., & Bassolo, V. (1998). *The Earth's*
749 *Plasmasphere* (1st ed.). Cambridge University Press.
750 <https://doi.org/10.1017/CBO9780511600098>

- 751 Lin, C. H., Richmond, A. D., Heelis, R. A., Bailey, G. J., Lu, G., Liu, J. Y., et al. (2005).
752 Theoretical study of the low- and midlatitude ionospheric electron density enhancement
753 during the October 2003 superstorm: Relative importance of the neutral wind and the
754 electric field. *Journal of Geophysical Research*, *110*(A12), A12312.
755 <https://doi.org/10.1029/2005JA011304>
- 756 Lin, D., Wang, W., Scales, W. A., Pham, K., Liu, J., Zhang, B., et al. (2019). SAPS in the 17
757 March 2013 Storm Event: Initial Results From the Coupled Magnetosphere-Ionosphere-
758 Thermosphere Model. *Journal of Geophysical Research: Space Physics*, *124*(7), 6212–
759 6225. <https://doi.org/10.1029/2019JA026698>
- 760 Lin, D., Sorathia, K., Wang, W., Merkin, V., Bao, S., Pham, K., et al. (2021). The role of diffuse
761 electron precipitation in the formation of subauroral polarization streams. *Journal of*
762 *Geophysical Research: Space Physics*. <https://doi.org/10.1029/2021JA029792>
- 763 Lin, D., Wang, W., Merkin, V., Bao, S., Sorathia, K., Pham, K., et al. (2022). Characterizing
764 auroral precipitation and ionospheric conductance with the Multiscale Atmosphere-
765 Geospace Environment model. *AGU Fall Meeting Abstracts, 2022*, SA24A-01.
- 766 Lin, D., Wang, W., Merkin, V. G., Huang, C., Oppenheim, M., Sorathia, K., et al. (2022). Origin
767 of Dawnside Subauroral Polarization Streams During Major Geomagnetic Storms. *AGU*
768 *Advances*, *3*(4). <https://doi.org/10.1029/2022AV000708>
- 769 Liu, J., Higuchi, T., Lyons, L. R., Ohtani, S., Wu, J., Zou, Y., et al. (2022). The Occurrence of
770 Embedded Region 1 and 2 Currents Depends on Geomagnetic Activity Level. *Journal of*
771 *Geophysical Research: Space Physics*, *127*(11). <https://doi.org/10.1029/2022JA030539>
- 772 Liu, Jing, Wang, W., Burns, A., Yue, X., Zhang, S., Zhang, Y., & Huang, C. (2016). Profiles of
773 ionospheric storm-enhanced density during the 17 March 2015 great storm. *Journal of*

- 774 *Geophysical Research: Space Physics*, 121(1), 727–744.
775 <https://doi.org/10.1002/2015JA021832>
- 776 Lu, G., Zakharenkova, I., Cherniak, I., & Dang, T. (2020). Large-Scale Ionospheric Disturbances
777 During the 17 March 2015 Storm: A Model-Data Comparative Study. *Journal of*
778 *Geophysical Research: Space Physics*, 125(5). <https://doi.org/10.1029/2019JA027726>
- 779 Ma, Q., Li, W., Zhang, X. -J., Bortnik, J., Shen, X. -C., Connor, H. K., et al. (2021). Global
780 Survey of Electron Precipitation due to Hiss Waves in the Earth's Plasmasphere and
781 Plumes. *Journal of Geophysical Research: Space Physics*, 126(8).
782 <https://doi.org/10.1029/2021JA029644>
- 783 Merkin, V. G., & Lyon, J. G. (2010). Effects of the low-latitude ionospheric boundary condition
784 on the global magnetosphere: IONOSPHERE/MAGNETOSPHERE GLOBAL
785 EFFECTS. *Journal of Geophysical Research: Space Physics*, 115(A10), n/a-n/a.
786 <https://doi.org/10.1029/2010JA015461>
- 787 Moldwin, M. B., Zou, S., & Heine, T. (2016). The story of plumes: the development of a new
788 conceptual framework for understanding magnetosphere and ionosphere coupling.
789 *Annales Geophysicae*, 34(12), 1243–1253. <https://doi.org/10.5194/angeo-34-1243-2016>
- 790 Pembroke, A., Toffoletto, F., Sazykin, S., Wiltberger, M., Lyon, J., Merkin, V., & Schmitt, P.
791 (2012). Initial results from a dynamic coupled magnetosphere-ionosphere-ring current
792 model. *Journal of Geophysical Research: Space Physics*, 117(A2), 2011JA016979.
793 <https://doi.org/10.1029/2011JA016979>
- 794 Pham, K. H., Zhang, B., Sorathia, K., Dang, T., Wang, W., Merkin, V., et al. (2022).
795 Thermospheric Density Perturbations Produced by Traveling Atmospheric Disturbances

- 796 During August 2005 Storm. *Journal of Geophysical Research: Space Physics*, 127(2).
797 <https://doi.org/10.1029/2021JA030071>
- 798 Pulkkinen, T. I., Tsyganenko, N. A., & Friedel, R. H. W. (Eds.). (2005). *The Inner*
799 *Magnetosphere: Physics and Modeling* (Vol. 155). Washington, D. C.: American
800 Geophysical Union. <https://doi.org/10.1029/GM155>
- 801 Qian, L., Burns, A. G., Emery, B. A., Foster, B., Lu, G., Maute, A., et al. (2014). The NCAR
802 TIE-GCM: A Community Model of the Coupled Thermosphere/Ionosphere System. In
803 Joseph Huba, R. Schunk, & G. Khazanov (Eds.), *Geophysical Monograph Series* (pp.
804 73–83). Chichester, UK: John Wiley & Sons, Ltd.
805 <https://doi.org/10.1002/9781118704417.ch7>
- 806 Raeder, J., Cramer, W. D., Jensen, J., Fuller-Rowell, T., Maruyama, N., Toffoletto, F., & Vo, H.
807 (2016). Sub-Auroral Polarization Streams: A complex interaction between the
808 magnetosphere, ionosphere, and thermosphere. *Journal of Physics: Conference Series*,
809 767, 012021. <https://doi.org/10.1088/1742-6596/767/1/012021>
- 810 Richmond, A. D., Ridley, E. C., & Roble, R. G. (1992). A thermosphere/ionosphere general
811 circulation model with coupled electrodynamics. *Geophysical Research Letters*, 19(6),
812 601–604. <https://doi.org/10.1029/92GL00401>
- 813 Sandel, B. R., King, R. A., Forrester, W. T., Gallagher, D. L., Broadfoot, A. L., & Curtis, C. C.
814 (2001). Initial results from the IMAGE Extreme Ultraviolet Imager. *Geophysical*
815 *Research Letters*, 28(8), 1439–1442. <https://doi.org/10.1029/2001GL012885>
- 816 Schunk, R. W., Banks, P. M., & Raitt, W. J. (1976). Effects of electric fields and other processes
817 upon the nighttime high-latitude *F* layer. *Journal of Geophysical Research*, 81(19),
818 3271–3282. <https://doi.org/10.1029/JA081i019p03271>

- 819 Tian, X., Yu, Y., Zhu, M., Ma, L., Cao, J., Pr, S., et al. (2022). Effects of EMIC Wave-Driven
820 Proton Precipitation on the Ionosphere. *Journal of Geophysical Research: Space Physics*,
821 *127*(2). <https://doi.org/10.1029/2021JA030101>
- 822 Toffoletto, F., Sazykin, S., Spiro, R., & Wolf, R. (2003). Inner magnetospheric mod-
823 eling with the rice convection model. *Space Science Reviews*, *107*(1/2), 175–196.
824 <https://doi.org/10.1023/A:1025532008047>
- 825 Wang, W., Talaat, E. R., Burns, A. G., Emery, B., Hsieh, S., Lei, J., & Xu, J. (2012).
826 Thermosphere and ionosphere response to subauroral polarization streams (SAPS):
827 Model simulations: THE EFFECT OF SAPS ON THE T-I SYSTEM. *Journal of*
828 *Geophysical Research: Space Physics*, *117*(A7), n/a-n/a.
829 <https://doi.org/10.1029/2012JA017656>
- 830 Wolf, R. A. (1983). The Quasi-Static (Slow-Flow) Region of the Magnetosphere. In R. L.
831 Carovillano & J. M. Forbes (Eds.), *Solar-Terrestrial Physics* (Vol. 104, pp. 303–368).
832 Dordrecht: Springer Netherlands. https://doi.org/10.1007/978-94-009-7194-3_14
- 833 Zhang, B., Lotko, W., Brambles, O., Wiltberger, M., & Lyon, J. (2015). Electron precipitation
834 models in global magnetosphere simulations. *Journal of Geophysical Research: Space*
835 *Physics*, *120*(2), 1035–1056. <https://doi.org/10.1002/2014JA020615>
- 836 Zhang, Binzheng, Sorathia, K. A., Lyon, J. G., Merkin, V. G., Garretson, J. S., & Wiltberger, M.
837 (2019). GAMERA: A Three-dimensional Finite-volume MHD Solver for Non-orthogonal
838 Curvilinear Geometries. *The Astrophysical Journal Supplement Series*, *244*(1), 20.
839 <https://doi.org/10.3847/1538-4365/ab3a4c>
- 840 Zou, S., Ridley, A. J., Moldwin, M. B., Nicolls, M. J., Coster, A. J., Thomas, E. G., &
841 Ruohoniemi, J. M. (2013). Multi-instrument observations of SED during 24-25 October

842 2011 storm: Implications for SED formation processes: SED FORMATION
843 PROCESSES. *Journal of Geophysical Research: Space Physics*, 118(12), 7798–7809.
844 <https://doi.org/10.1002/2013JA018860>

845 Zou, S., Moldwin, M. B., Ridley, A. J., Nicolls, M. J., Coster, A. J., Thomas, E. G., &
846 Ruohoniemi, J. M. (2014). On the generation/decay of the storm-enhanced density
847 plumes: Role of the convection flow and field-aligned ion flow: Generation and Decay of
848 SED Plumes. *Journal of Geophysical Research: Space Physics*, 119(10), 8543–8559.
849 <https://doi.org/10.1002/2014JA020408>

850 Zou, Y., Walsh, B. M., Shi, X., Lyons, L., Liu, J., Angelopoulos, V., et al. (2021). Geospace
851 Plume and Its Impact on Dayside Magnetopause Reconnection Rate. *Journal of*
852 *Geophysical Research: Space Physics*, 126(6). <https://doi.org/10.1029/2021JA029117>
853